Model Predictive Current Control of Traction Permanent Magnet Synchronous Motors in Six-Step Operation for Railway Application

Xiaochun Fang, *Member*, *IEEE*, Shuai Lin, *Student Member*, *IEEE*, Xiaofan Wang, Zhongping Yang, *Member*, *IEEE*, Fei Lin, *Member*, *IEEE*, and Zhongbei Tian, *Member*, *IEEE*

***Abstract*—This paper proposes a finite set model predictive current control scheme for traction permanent magnet synchronous motors for railway application. For the rail transit drive system, it is necessary to realize the six-step operation. A method based on voltage vector clamping is presented to realize overmodulation including six-step operation and maximize the utilization ratio of dc voltage. The essence of voltage vector clamping is to gradually reduce the space of action of the closed-loop regulation mechanism until it enters six-step operation. This method is simple and feasible, which does not need to add controllers or switch the control framework. An ideal voltage vector reference coordinate system is established to analyze the current trajectory under different modulation ratios. Thus, an optimal control strategy in the ideal voltage reference coordinate system is proposed. Experiments are conducted to prove that six-step operation can be achieved and this strategy has an obvious effect on switching frequency index in the overmodulation area.**

***Index Terms*—Permanent magnet synchronous motor (PMSM), model predictive control (MPC), six-step mode, voltage vector clamping**

I. Introduction

THERE is a great application prospect for permanent magnet synchronous motor (PMSM) in rail transit due to its high efficiency and high power density [1]. The control technology of PMSM directly affects the operation performance of trains. Many advanced control methods have been proposed to improve PMSM performance in recent years [2]-[5]. Among them, model predictive control (MPC) has received extensive attention due to its superior dynamic response and intuitive implementation. However, for rail transit applications, the classical linear control methods with many limitations, such as proportional-integral field oriented control (FOC) based on pulse width modulation (PWM), are still the mainstreams in practical applications [1].

For the rail transit drive system, it is necessary to realize the six-step operation. Above the base speed, limited by the output voltage of the inverter, the motor needs to be controlled by the flux-weakening control scheme. At this time, the inverter usually adopts six-step operation to improve the voltage utilization ratio. In the overmodulation area, the current harmonics increase due to voltage saturation, which will lead to poor and unstable control performance.

The overmodulation method based on space vector PWM (SVPWM) has been studied for decades [6], [7]. MPC can be divided into continuous set MPC (CS-MPC) and finite set MPC (FS-MPC). CS-MPC usually needs to use a modulator. Reference [8], [9] combined PWM with MPC and achieved overmodulation, but the six-step operation problems have not been considered. In [10], a harmonic reference generator (HRG) was combined with CS-MPC to realize overmodulation including six-step operation. FS-MPC takes into account the discrete characteristics of devices and directly outputs the switching state for the inverter. Although the operation area was expanded by FS-MPC in [11]-[13], it did not enter six-step mode. In [14], the switching frequency weight factor was set a large value to enter six-step operation. The large value caused poor current harmonic performance. Thus, the large value of weight factor could not be applied in low speed area and the switching frequency weighting factor needed to be changed with the operation speed. Holtz proposed the use of a rectangular current boundary to realize the six-step mode operation [6], [15], [16]. However, the method was for induction motor (IM). Due to the limited computing ability of the microprocessor at that time, the induction motor model was greatly simplified [15]. In [17], model predictive torque control (MPTC) is applied to realize six-step operation. However, while low harmonic current distortion ensures low torque ripple, achieving low torque ripple does not necessarily entail low current distortion [16]. In railway traction drive system, torque ripple and current distortion are two important performance indexes. Thus, model predictive current control (MPCC) is preferred in railway application.

This paper proposes an FS-MPCC method for PMSM to achieve overmodulation including six-step operation. The

This work was supported by "the Fundamental Research Funds for the Central Universities" (2019JBM061). *(Corresponding author: Xiaochun Fang, Shuai Lin.)*

X. Fang, S. Lin, Z. Yang, and F. Lin are with the Beijing Jiaotong University, Beijing, 100044, China (e-mail: fangxc@bjtu.edu.cn; ShuaiLin@bjtu.edu.cn; zhpyang@bjtu.edu.cn; flin@bjtu.edu.cn).

X. Wang is with Locomotive & Car Research Institute, China Academy of Railway Sciences Corporation Limited, Beijing, 100081, China (e-mail: wangxiaofan@zemt.cn).

Z. Tian is with the University of Liverpool, Liverpool, U.K. (e-mail: Zhongbei.Tian@liverpool.ac.uk).

method is simple and easy to implement and does not need to add an additional regulator or switch the control framework. The structure of this paper is arranged as follows. Section II introduces the basic control framework of FS-MPCC. The control scheme to achieve overmodulation including six-step mode is described in Section III. In Section IV, an innovative coordinate system is established to analyze the current trajectory and an optimal MPCC control strategy is proposed. Section V shows the experimental investigations and Section VI gives the conclusion.

II. Model Predictive Control Framework of PMSM Traction System

The MPCC strategy is implemented based on the mathematical models of the inverter and the PMSM. In order to evaluate the control performance of the stator current, the errors e of stator current in dq axis are defined as:

$$\begin{cases} e_{i,\mathrm{sd}}^{\mathrm{pre}}(t) = i_{\mathrm{sd}}^{\mathrm{ref}}(t) - i_{\mathrm{sd}}^{\mathrm{pre}}(t) \\ e_{i,\mathrm{sq}}^{\mathrm{pre}}(t) = i_{\mathrm{sq}}^{\mathrm{ref}}(t) - i_{\mathrm{sq}}^{\mathrm{pre}}(t) \end{cases} \tag{1}$$

$i_{\mathrm{sd}}{}^{\mathrm{ref}}$ and $i_{\mathrm{sq}}{}^{\mathrm{ref}}$ are the reference values of current. $i_{\mathrm{sd}}{}^{\mathrm{pre}}$ and $i_{\mathrm{sq}}{}^{\mathrm{pre}}$ are the predicted values of current.

When the voltage vector $\boldsymbol{v}_k(t_0)$ is applied, the linearization method can be used to approximate the trajectory of the future current error as (2). k is the index of voltage vector. t_0 is the current time.

$$\begin{cases} e_{i,\mathrm{sd}}^{\mathrm{pre}}(t,k) = e_{i,\mathrm{sd}}(t_0) + \left.\dfrac{\mathrm{d}e_{i,\mathrm{sd}}^{\mathrm{pre}}(t,k)}{\mathrm{d}t}\right|_{t_0} \Delta t \\ e_{i,\mathrm{sq}}^{\mathrm{pre}}(t,k) = e_{i,\mathrm{sq}}(t_0) + \left.\dfrac{\mathrm{d}e_{i,\mathrm{sq}}^{\mathrm{pre}}(t,k)}{\mathrm{d}t}\right|_{t_0} \Delta t \end{cases} \tag{2}$$

It is assumed that the reference current change rate is zero in steady state. According to (1), (2) and motor voltage equation in dq reference coordinate system, the current errors can be expressed as (3) after a sampling period, that is, when $t = t_0+T_\mathrm{c}$. To compensate for the existence of a delay in the actual system, (3) can be rewritten as (4), which is the prediction model used in this paper.

$$\begin{aligned} e_{i,\mathrm{sd}}^{\mathrm{pre}}(t_0+T_\mathrm{c},k) &= e_{i,\mathrm{sd}}(t_0) - [u_{\mathrm{sd}}(t_0,k) - R_\mathrm{s} i_{\mathrm{sd}}(t_0) \\ &\quad + \omega_\mathrm{r} L_{\mathrm{sq}} i_{\mathrm{sq}}(t_0)] \frac{T_\mathrm{c}}{L_{\mathrm{sd}}} \\ e_{i,\mathrm{sq}}^{\mathrm{pre}}(t_0+T_\mathrm{c},k) &= e_{i,\mathrm{sq}}(t_0) - [u_{\mathrm{sq}}(t_0,k) - R_\mathrm{s} i_{\mathrm{sq}}(t_0) \\ &\quad - \omega_\mathrm{r} L_{\mathrm{sd}} i_{\mathrm{sd}}(t_0) - \omega_\mathrm{r}\psi_\mathrm{f}] \frac{T_\mathrm{c}}{L_{\mathrm{sq}}} \end{aligned} \tag{3}$$

$$\begin{aligned} e_{i,\mathrm{sd}}^{\mathrm{pre}}(t_0+2T_\mathrm{c},k) &= e_{i,\mathrm{sd}}(t_0+T_\mathrm{c}) - [u_{\mathrm{sd}}(t_0+T_\mathrm{c},k) - R_\mathrm{s} i_{\mathrm{sd}}(t_0+T_\mathrm{c}) \\ &\quad + \omega_\mathrm{r} L_{\mathrm{sq}} i_{\mathrm{sq}}(t_0+T_\mathrm{c})] \frac{T_\mathrm{c}}{L_{\mathrm{sd}}} \\ e_{i,\mathrm{sq}}^{\mathrm{pre}}(t_0+2T_\mathrm{c},k) &= e_{i,\mathrm{sq}}(t_0+T_\mathrm{c}) - [u_{\mathrm{sq}}(t_0+T_\mathrm{c},k) - R_\mathrm{s} i_{\mathrm{sq}}(t_0+T_\mathrm{c}) \\ &\quad - \omega_\mathrm{r} L_{\mathrm{sd}} i_{\mathrm{sd}}(t_0+T_\mathrm{c}) - \omega_\mathrm{r}\psi_\mathrm{f}] \frac{T_\mathrm{c}}{L_{\mathrm{sq}}} \end{aligned} \tag{4}$$

i_{sd} and i_{sq} are the actual values of current obtained by sampling. T_c is the control period (sampling period). R_s is the stator resistance. L_d and L_q are inductances in dq axis. ω_r is the rotor angular velocity. u_{sd} and u_{sq} are the stator voltages in dq axis. ψ_f is the rotor flux.

Then, the cost function J is denoted in (5).

$$J(t,k) = e_{i,\mathrm{sd}}^{\mathrm{pre}\,2}(t,k) + e_{i,\mathrm{sq}}^{\mathrm{pre}\,2}(t,k) + \lambda_{\mathrm{sw}} n_{\mathrm{sw}}(t,k) \tag{5}$$

In (5), $e_{i,\mathrm{sd}}{}^{\mathrm{pre}\,2}$ and $e_{i,\mathrm{sq}}{}^{\mathrm{pre}\,2}$ are squares of predicted current error. n_{sw} is the switching times in each control period. λ_{sw} is the switching frequency penalty coefficient. In railway application, onboard traction converters usually bear high voltage and large current. Consequently, the switching frequency is limited to reduce switching loss, which should be one of the control targets [17].

Finally, the optimal voltage vector $\boldsymbol{v}_k{}^{\mathrm{opt}}$ is the voltage vector among the finite control set that makes the cost function J minimum. The control set applied is shown in TABLE I.

$$\boldsymbol{v}_k^{\mathrm{opt}}(t_0+T_\mathrm{c}) = \arg \underset{\boldsymbol{v}_k(t_0+T_\mathrm{c})}{\text{minimize}}\ J(t_0+2T_\mathrm{c},k) \tag{6}$$

TABLE I
Control Set of MPCC

Current voltage vector	Switch state (S_a S_b S_c)	Preselected voltage vector set for the next sampling period
$\boldsymbol{v_0}$	(0 0 0)	{$\boldsymbol{v_0}$ $\boldsymbol{v_1}$ $\boldsymbol{v_3}$ $\boldsymbol{v_5}$}
$\boldsymbol{v_1}$	(1 0 0)	{$\boldsymbol{v_1}$ $\boldsymbol{v_6}$ $\boldsymbol{v_2}$ $\boldsymbol{v_0}$}
$\boldsymbol{v_2}$	(1 1 0)	{$\boldsymbol{v_2}$ $\boldsymbol{v_1}$ $\boldsymbol{v_3}$ $\boldsymbol{v_7}$}
$\boldsymbol{v_3}$	(0 1 0)	{$\boldsymbol{v_3}$ $\boldsymbol{v_2}$ $\boldsymbol{v_4}$ $\boldsymbol{v_0}$}
$\boldsymbol{v_4}$	(0 1 1)	{$\boldsymbol{v_4}$ $\boldsymbol{v_3}$ $\boldsymbol{v_5}$ $\boldsymbol{v_7}$}
$\boldsymbol{v_5}$	(0 0 1)	{$\boldsymbol{v_5}$ $\boldsymbol{v_4}$ $\boldsymbol{v_6}$ $\boldsymbol{v_0}$}
$\boldsymbol{v_6}$	(1 0 1)	{$\boldsymbol{v_6}$ $\boldsymbol{v_5}$ $\boldsymbol{v_1}$ $\boldsymbol{v_7}$}
$\boldsymbol{v_7}$	(1 1 1)	{$\boldsymbol{v_7}$ $\boldsymbol{v_2}$ $\boldsymbol{v_4}$ $\boldsymbol{v_6}$}

In TABLE I, $\boldsymbol{v}_k$ (k = 0, 1, 2, …, 7) is the basic voltage vector of the inverter. S_x (x = a, b, c) is the switch state of the inverter, and it is defined as

$$S_x = \begin{cases} 1, \text{ if the upper switch is closed} \\ 1, \text{ if the upper switch is open} \end{cases} \quad (x = \mathrm{a,b,c}) \tag{7}$$

The preselected voltage vector set in TALBE I is applied as the control set. The control set includes current voltage vector and three adjacent voltage vectors. By applying the control set, the average switching frequency of the power devices will be less than 1/6 of the sampling frequency.

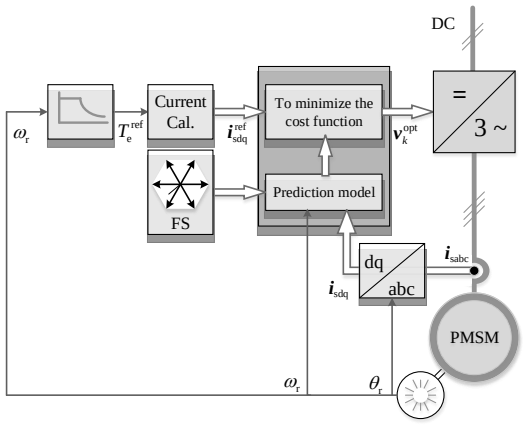

Fig. 1. Block diagram of model predictive current control.

Then, the basic framework of MPCC is shown in Fig. 1. The prediction model and the cost function are the most important parts, which affect the control performance. Based on the prediction model, the future current trajectory is predicted. The

cost function is used to evaluate the predicted results and select the optimal voltage vector $\boldsymbol{v}_k^{\text{opt}}$ to realize the current closed-loop control. In the current calculation module, the maximum torque per ampere (MTPA) control is employed below the base speed and flux-weakening control is applied in six-step operation.

Besides, the switching frequency is calculated indirectly according to the total switching times of the inverter over a period of time. Within N sampling cycles, the total switching times of the inverter are summed. The average switching frequency f_{sw} is defined as (8).

$$f_{\text{sw}} = \lim_{N\to\infty} \frac{1}{6NT_{\text{c}}} \sum_{x=\text{a,b,c}} \sum_{l=1}^{N} \left| S_x(t_0 + lT_{\text{c}}) - S_x(t_0 + lT_{\text{c}} - T_{\text{c}}) \right| \quad (8)$$

III. Control Scheme to Achieve Overmodulation Including Six-Step Operation

In MPC, the flux-weakening control scheme can be achieved by substituting the current reference value into the cost function. The current reference value is calculated based on the current trajectory in flux-weakening area. The flux-weakening control can also be achieved by integrating the voltage limitation equation into the cost function. However, due to the influence of motor parameters, the actual current reference value is often different from the calculated result. To avoid current out of control, a certain voltage margin needs to be reserved, so it is difficult to realize six-step mode operation and the voltage utilization ratio is low.

FS-MPC does not generate voltage reference or use the modulation module. The concepts of ideal voltage vector u_{s}^* and equivalent modulation ratio M are introduced for the convenience of description. In the case of no static difference in current tracking, the actual current value fluctuates around the reference value. The current reference value can be substituted into the PMSM voltage equation to calculate the ideal voltage vector u_{s}^*. u_{s}^* should be the same as the output voltage fundamental wave of the inverter AC side. The DC-link voltage of the inverter is $2U_{\text{dc}}$. The phase voltage of the inverter AC side is u_1. Thus, the equivalent modulation ratio M is defined as

$$M = \frac{u_1}{U_{\text{dc}}} = \frac{u_{\text{s}}^*}{U_{\text{dc}}} \quad (9)$$

The linear modulation range is $0 \le M \le 1.15$. The output fundamental wave amplitude of the inverter in six-step mode is $u_{1,\max} = (4/\pi)U_{\text{dc}} = 1.273U_{\text{dc}}$. Therefore, the maximum output voltage amplitude of the inverter can be increased by about 10.7% by entering the nonlinear control range, which is the overmodulation area $1.15 < M \le 1.273$.

To realize overmodulation including six-step operation and maximize the utilization of DC voltage, the saturation problem of the current regulator must be solved. Due to the independent regulation of the double current closed-loop controller, two degrees of freedom are required. After entering six-step mode, the adjustment freedom degree of the output voltage changes from two (amplitude and phase) to one (phase), which is the fundamental reason for saturation.

An overmodulation method based on voltage vector clamping is proposed to solve the problem of insufficient freedom degree. As shown in Fig. 2, according to M, the original sectors are redivided, including six clamping areas and six free areas. The clamping area is a central symmetric distribution based on the angle of the basic voltage vector v_k with a width of $2\alpha_{\text{ov}}$. The gap in the clamping area is the free area and the width is $\pi/3\text{-}2\alpha_{\text{ov}}$. u_{s}^* and M are calculated based on the current reference value, and the angle α_{ov} is calculated as (10).

$$\alpha_{\text{ov}} = \begin{cases} 0, & M \le 1.212 \\ \dfrac{\pi}{6}\dfrac{M-1.212}{1.273-1.212}, & 1.212 < M < 1.273 \\ \dfrac{\pi}{6}, & M \ge 1.273 \end{cases} \quad (10)$$

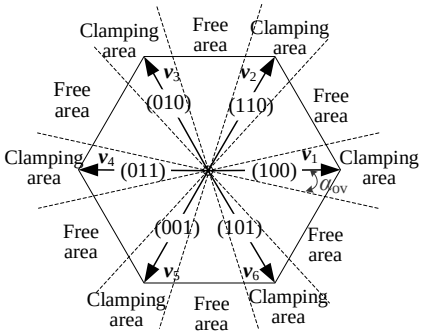

Fig. 2. Schematic diagram of basic voltage vector clamping.

When u_{s}^* is located in the clamping area of $\boldsymbol{v}_k$, $\boldsymbol{v}_k$ is executed regardless of the result obtained by minimizing the cost function. In the free area, the double current closed-loop mechanism is still maintained. The optimal voltage vector v_k^{opt} is executed, which is obtained by minimizing the cost function. The reason why the voltage vector clamping is started from M = 1.212 is that M = 1.212 is the equivalent modulation ratio when the ideal voltage vector trajectory moves completely along the edge of the hexagon. When M > 1.212, the optimal voltage vector is only selected from the non-zero voltage vectors, and the zero vectors are no longer used. When $M \ge 1.273$, the free areas disappear and the six basic voltage vectors switch successively, that is six-step mode.

Thus, MPCC with voltage vector clamping is applied for PMSM to achieve overmodulation including six-step. Fig. 3 shows the algorithm of MPCC with voltage vector clamping.

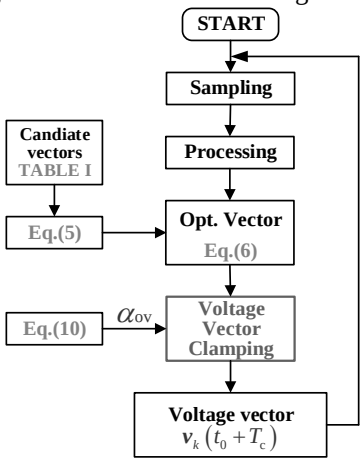

Fig. 3. Algorithm of MPCC with voltage vector clamping.

IV. Optimal MPCC Based on Current Boundary from Overmodulation to Six-Step Operation

A. The Establishment of The Ideal Voltage Reference Coordinate System

The change of stator current depends on the difference between the real voltage vector and the ideal voltage vector. When PMSM operates at different operation points, the amplitude and angle in the d-q coordinate system are also different. In order to facilitate the analysis of the variation law of current ripple, this paper establishes a voltage reference coordinate system (x-y). The ideal voltage vector u_s^* lags the positive x-axis by 90 degrees and the positive direction of u_s^* is at the positive y-axis, as shown in Fig. 4. In this coordinate system, the ideal voltage vector always coincides with the y-axis, and only the amplitude changes. The actual voltage vector is selected from the eight basic voltage vectors of the inverter. According to the volt-second balance principle, the average value of v_k is consistent with u_s^*.

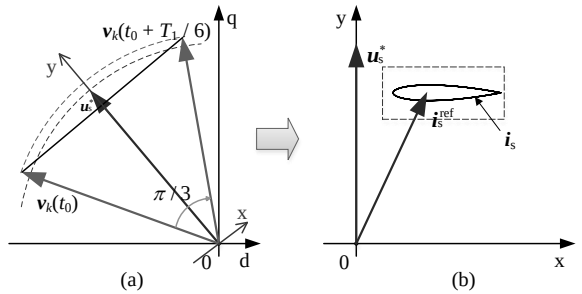

Fig. 4. Establishment of reference voltage coordinate system. (a) The d-q coordinate system. (b) The x-y coordinate system.

B. Current Boundary Shape Optimization Based on Current Trajectory Characteristics

In six-step mode, the six non-zero fundamental voltage vectors of the inverter are switched in turn, and the duration of each voltage vector is one sixth of the fundamental period. The ideal voltage vector amplitude is $1.273U_{dc}$, and the actual voltage vector amplitude is $4U_{dc}/3$. In the synchronous rotation coordinate system (d-q), the ideal voltage vector at the steady state remains unchanged. After one sixth of the fundamental period, the voltage is rotated clockwise by an electric angle of $\pi/3$. The range of angle between v_k and the y-axis is

$$\theta_{ky}=\omega_r t,\ \theta_{ky}\in(-\pi/6,\ \pi/6] \tag{11}$$

The x and y components of the difference vector $\boldsymbol{e}_{u,s}$ between the actual voltage vector v_k and the ideal voltage vector u_s^* are

$$\begin{aligned} e_{u,sx} &= \frac{4}{3}U_{dc}\sin(\theta_{ky}) \\ e_{u,sy} &= \frac{4}{3}U_{dc}\cos(\theta_{ky})-u_s^* \end{aligned} \tag{12}$$

The variation curve of voltage difference $e_{u,sx}$ and $e_{u,sy}$ within a fundamental period is shown in Fig. 5. The fluctuation period is one sixth of the fundamental period, and the fluctuation amplitude of $e_{u,sx}$ is larger than $e_{u,sy}$. For the convenience of analysis, the difference between the inductance of d-axis and q-axis is temporarily ignored, that is $L_d = L_q = L_s$. Then the x and y components of the ripple current $e_{i,s}$ are

$$\begin{aligned} e_{i,sx} &= \frac{1}{L_s}\int\frac{4U_{dc}}{3}\sin(\theta_{ky})dt \\ e_{i,sy} &= \frac{1}{L_s}\int\left(\frac{4U_{dc}}{3}\cos(\theta_{ky})-u_s^*\right)dt \end{aligned} \tag{13}$$

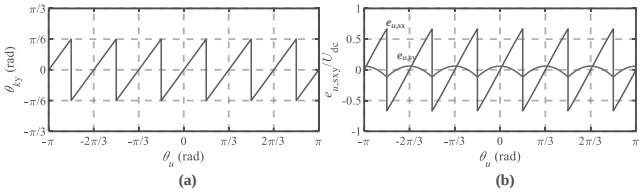

Fig. 5. Difference between actual voltage vector and ideal voltage vector in six-step mode. (a) Angle difference. (b) The component in the x-axis and the y-axis.

If DC voltage $2U_{dc}$ =200V and L_s=0.004H, the current error waveform within a fundamental wave period can be drawn, as shown in Fig. 6. Same as the law of voltage error, the period of fluctuation is one sixth of the fundamental period, and the fluctuation amplitude of $e_{i,sx}$ is larger than $e_{i,sy}$. In the x-y coordinate system, the trajectory of $e_{i,s}$ is a horizontal water drop shape.

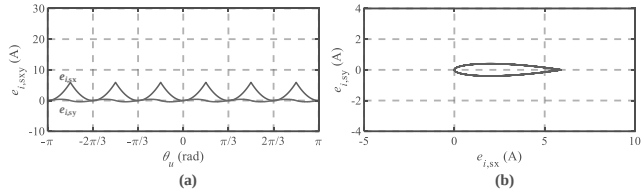

Fig. 6. Current error in six-step mode and its trajectory in x-y coordinate system. (a) The component in the x-axis and the y-axis. (b) The trajectory in the x-y coordinate system.

When the amplitude of the ideal voltage vector is less than $1.273U_{dc}$, the current trajectory will change assuming that the inverter is still operating in six-step mode. The average value of the x-axis component of the voltage error is still zero, but the y-axis component will shift upward and the average value is greater than zero. When the amplitude of the ideal voltage vector is less than $1.15U_{dc}$, the y-axis component of the voltage vector difference is always larger than zero. The voltage error curves at M = 1.212 and M = 1.15 are respectively drawn in Fig. 7. The y-axis voltage error whose average value is larger than zero will cause the current error to accumulate in the y-axis direction, so the current reference tracking cannot be realized. The current error curves at M = 1.212 and M = 1.15 and their trajectories in the x-y coordinate system are shown in Fig. 8 and Fig. 9, respectively.

The current error of six-step mode is analyzed in the x-y coordinate system, and the following three points are summarized: (1) When the modulation ratio M = 1.273, under the action of six-step voltage, the current error presents a horizontal water drop shape, and the fluctuation range of the x-axis is larger than the y-axis. (2) When the modulation ratio is 1.15< M <1.273, the fluctuation range of current error in the x-axis direction remains unchanged, but error accumulation will occur in the y-axis direction. The smaller the modulation ratio is, the faster the drift speed of the current trajectory in the y-axis direction is. (3) When $M \le 1.15$, the current error of the y-axis direction increases monotonically, and the fluctuation

range of the x-axis current error is no longer significantly larger than the y-axis direction. The above analysis assumes that the inverter works in the six-step mode. In fact, when the modulation ratio is less than 1.273, it must quit the six-step mode and move the current trajectory to the y-axis negatively by switching the switching state to avoid the accumulation of current error. Although the conclusions are obtained based on the assumption that $L_d = L_q$, they are still true when $L_d < L_q$.

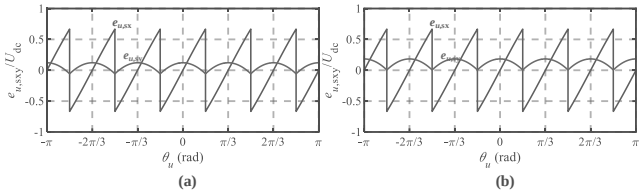

Fig. 7. Voltage error in six-step mode. (a) M = 1.212. (b) M = 1.15.

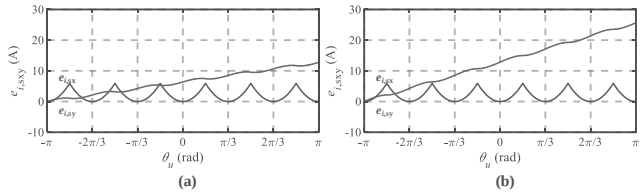

Fig. 8. Current error in six-step mode. (a) M = 1.212. (b) M = 1.15.

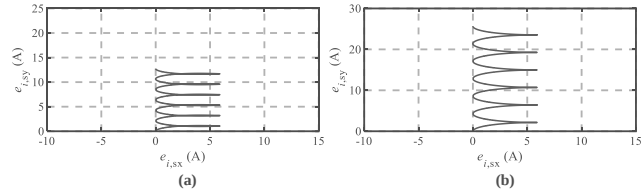

Fig. 9. Trajectory of current error in x-y coordinate system. (a) M = 1.212. (b) M = 1.15.

In the x-y coordinate system, the x-axis component of the overmodulation ripple current is much larger than the y-axis component. The contact number between the left and right sides of the limiting boundary will be significantly more than that between the upper and lower sides. Therefore, this paper draws a rectangular boundary in the x-y coordinate system. The long side of the rectangle is parallel to the x-axis and the short side is parallel to the y-axis. The rectangular boundary can adapt to the characteristics of the ripple current in the overmodulation area. It can also reduce the contact number between current trajectory and boundary, thus further reducing switching frequency. In the linear area, the circular boundary is applied. The size of the circular boundary is expressed by the radius $e_{i,\mathrm{sw}}$, which can also reflect the limitation of switching frequency. The optimal voltage vector for each sampling period in the linear area is

$$\boldsymbol{v}_k^{\mathrm{opt}}(t_0+T_\mathrm{c}) = \begin{cases} \boldsymbol{v}_k^{\mathrm{opt}}(t_0) & , e_{i,\mathrm{s}}^{\mathrm{pre}}\left(t_0+2T_\mathrm{c}, k(t_0)\right) \le e_{i,\mathrm{sw}} \\ \underset{\boldsymbol{v}_k(t_0+T_\mathrm{c})}{\arg\ \text{minimize}}\ J(t_0+2T_\mathrm{c}, k) & , e_{i,\mathrm{s}}^{\mathrm{pre}}\left(t_0+2T_\mathrm{c}, k(t_0)\right) > e_{i,\mathrm{sw}} \end{cases} \quad (14)$$

In the overmodulation area, the rectangular boundary is applied. The long side of the rectangular boundary is $2e_{i,\mathrm{swx}}$ and the short side is $2e_{i,\mathrm{swy}}$. The optimal voltage vector for each sampling period in the overmodulation area is

$$\boldsymbol{v}_k^{\mathrm{opt}}(t_0+T_\mathrm{c}) = \begin{cases} \boldsymbol{v}_k^{\mathrm{opt}}(t_0) & , \begin{cases} e_{i,\mathrm{sx}}^{\mathrm{pre}}\left(t_0+2T_\mathrm{c}, k(t_0)\right) \le e_{i,\mathrm{swx}} \\ \text{and } e_{i,\mathrm{sy}}^{\mathrm{pre}}\left(t_0+2T_\mathrm{c}, k(t_0)\right) \le e_{i,\mathrm{swy}} \end{cases} \\ \underset{\boldsymbol{v}_k(t_0+T_\mathrm{c})}{\arg\ \text{minimize}}\ J(t_0+2T_\mathrm{c}, k) & , \begin{cases} e_{i,\mathrm{sx}}^{\mathrm{pre}}\left(t_0+2T_\mathrm{c}, k(t_0)\right) > e_{i,\mathrm{swx}} \\ \text{or } e_{i,\mathrm{sy}}^{\mathrm{pre}}\left(t_0+2T_\mathrm{c}, k(t_0)\right) > e_{i,\mathrm{swy}} \end{cases} \end{cases} \quad (15)$$

The optimal MPCC control strategy is based on current boundary and voltage vector clamping. Fig. 10 describes how to achieve overmodulation including six-step operation by optimal MPCC control strategy. The penalty coefficient of switching frequency λ_{sw} is 0. The switching frequency is limited by the current boundary. The circular current boundary is used in the linear area, and the rectangular current boundary is used after entering the overmodulation area I and II. The optimal vector selected by minimizing the cost function is performed in the linear area and the overmodulation area I. After entering the overmodulation area II, the angle α_{ov} of the voltage clamping area is gradually increased until $\alpha_{\mathrm{ov}} = \pi/6$ in six-step mode.

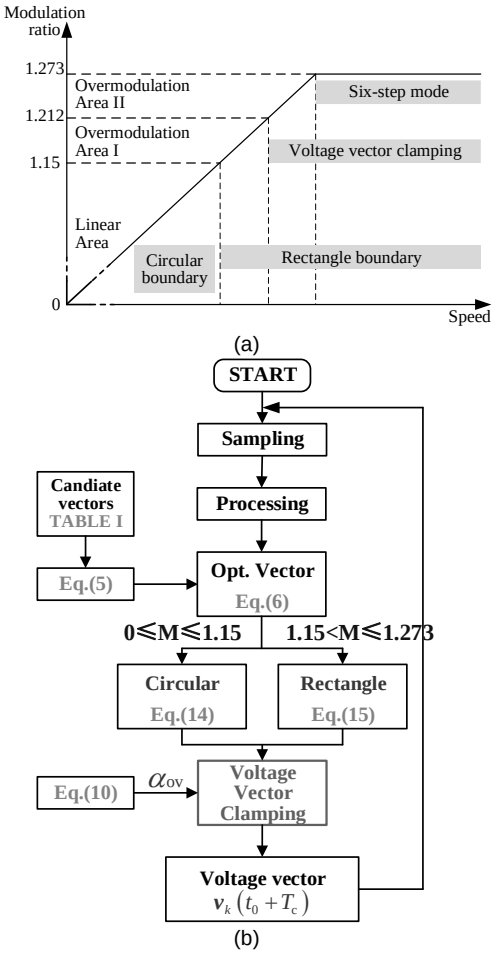

Fig. 10. Optimal MPCC control strategy based on current boundary in full speed domain. (a) Schematic diagram. (b) Algorithm.

V. Experiments

A. Experimental Platform

The experiment platform is shown in Fig. 11. It is composed of an induction motor and a PMSM. The two motors are

connected by a coupling. A torquemeter is installed to measure the output torque of the motor. A flywheel is installed to simulate the inertial load of the railway vehicle.

The topology of the experimental platform is shown in Fig. 12. In the experiment, PMSM driven by inverter 1 is used as the traction motor. The dSPACE real-time simulation system is used as the controller of inverter 1. The ControlDesk software supporting dSPACE is used to compile and download the control algorithm, monitor the experimental process, collect and store the data, and so on. The induction motor is driven by inverter 2 as the test system. Inverters 1 and 2 are derived from AC-DC-AC converters. Each converter contains a diode three-phase rectifier bridge, an IGBT two-level three-phase inverter and DC-link capacitors. Since the diode rectifier bridge cannot realize the electric braking energy feedback, the DC-links of two AC-DC-AC converters are connected. The three-phase power supply of 380V and 50Hz is converted by the transformer as the AC input of one of the AC-DC-AC converter.

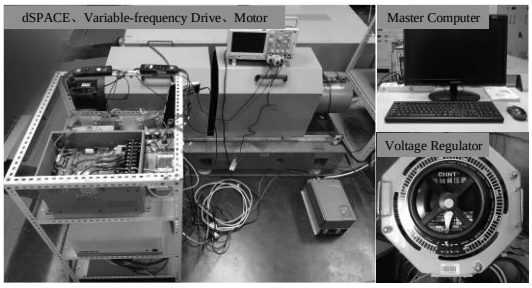

Fig. 11. 4.4 kW experimental platform.

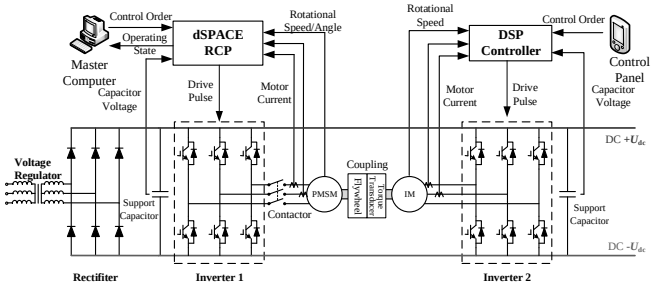

Fig. 12. The topology of 4.4 kW experimental platform.

TABLE I
PARAMETERS OF PMSM TRACTION SYSTEM

Parameter	Value	Parameter	Value
Rated power /kW	4.4	Magnetic flux linkage /Wb	0.181
Rated speed/rpm	1500	Stator resistance /Ω	0.3
Rated frequency/Hz	125	d-axis inductance /H	0.004
Rated torque/N·m	28.4	q-axis inductance /H	0.0045
Rated voltage/V	380	Pole pair	5
Rated current/A	16.5	DC side voltage /V	200

The parameters of PMSM are shown in TABLE I. Due to the small permanent magnet flux of PMSM, it requires a very high speed to enter the flux-weakening control scheme at rated voltage. Due to the limitation of laboratory space, in order to ensure safety, the DC-link voltage of the inverter is adjusted to $2U_{dc}$ = 200 V. The rated frequency of PMSM is about 80 Hz and the rated speed is 960 rpm calculated according to no-load back electromotive force. The sampling frequency is 40kHz. The experimental condition is that PMSM is under traction operation state with full torque output. And the experimental results show the control performance of PMSM in full speed range.

B. MPCC without Voltage Vector Clamping

The MPCC method is adopted, and the penalty coefficient of switching frequency λ_{sw} is 2.5. The experimental results are shown in Fig. 13. The average switching frequency in the overmodulation area is between 300-400Hz. According to (9), M is calculated from ideal voltage vector u^*, and u^* is calculated from current reference. Thus, M can reach $4/\pi$. However, six-step operation is never entered. Besides, there is a significant static difference between the actual current (red and blue solid lines) and the reference value (black dotted lines) after entering the overmodulation area, indicating saturation problem of current closed-loop control. In particular, the q-axis current is obviously small in the $9 < t < 20$ s, which will lead to insufficient torque output. It should be noticed that the current reference value in the experiment fluctuates, which is due to the real-time sampling of DC voltage and speed information used in the calculation process.

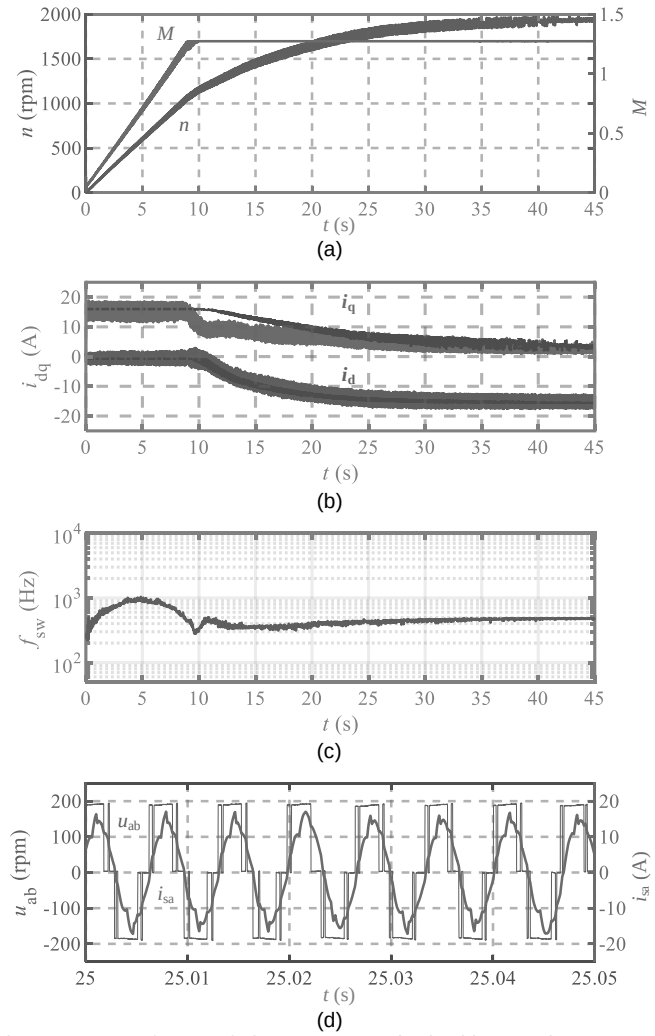

Fig. 13. Waveforms of the MPCC method without voltage vector clamping. (a) The speed n and modulation ratio M. (b) The dq-axis current i_{dq}. (c) The switching frequency f_{sw}. (c) The line voltage u_{ab} and phase current i_{sa}.

C. MPCC with Voltage Vector Clamping

Based on MPCC, the voltage vector clamping strategy is added in overmodulation, which is described in Section III. The penalty coefficient of switching frequency λ_{sw} is 2.5. The experimental results are shown in Fig. 14.

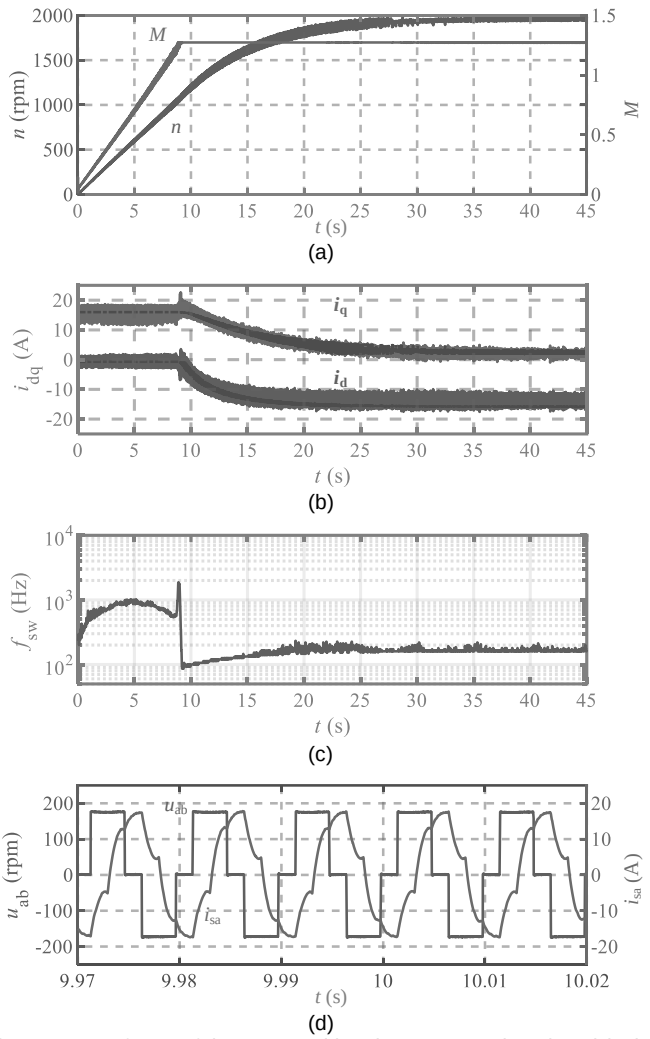

Fig. 14. Waveforms of the MPCC with voltage vector clamping. (a) The speed n and modulation ratio M. (b) The dq-axis current i_{dq}. (c) The switching frequency f_{sw}. (c) The line voltage u_{ab} and phase current i_{sa}.

When t > 9s, the average switching frequency decreases to the fundamental frequency, indicating that six-step mode has been successfully entered at this time. Besides, even in the case of fluctuation of the reference value, the current tracking error is still small, which ensures the torque output capacity in the full speed range. However, compared with MPCC without voltage vector clamping, the switching frequency of MPCC with voltage vector clamping increases significantly (about 1950Hz) in a small overmodulation area (8 < t < 9 s) before entering six-step mode.

D. Optimal MPCC Based on Current Boundary

To further improve the performance of the overmodulation area, the optimal MPCC based on current boundary is applied, which is described in Section IV. The penalty coefficient of switching frequency λ_{sw} is 0. The switching frequency is limited by the current boundary. In the linear area, the circular current boundary is applied and $e_{i,sw}$ = 2.25A. The rectangular current boundary is used instead of the circular current boundary when the modulation ratio is greater than 1.15. In the ideal voltage reference coordinate system, the rectangular boundary parameters are $e_{i,swx}$ = 2.75, $e_{i,swy}$ = 1.75A. The long and short sides are 5.5A and 3.5A, respectively. Fig. 15 shows the experimental results in the full speed range. It can be seen that the switching frequency in the overmodulation area can be reduced by using the rectangular boundary when entering the six-step mode, but the control effect is not affected.

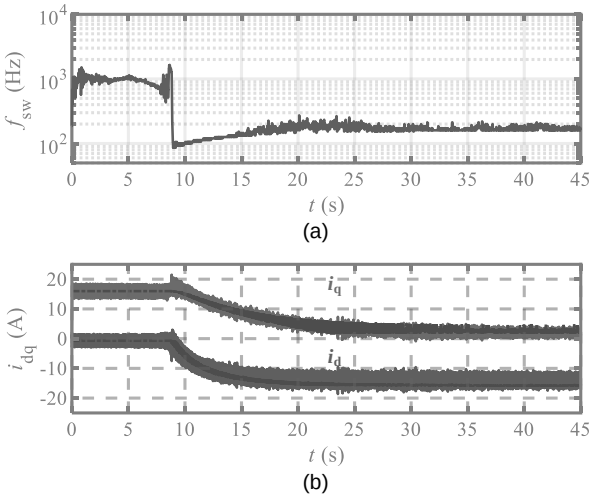

Fig. 15. Waveforms of the optimal MPCC with voltage vector clamping and rectangular bounds. (a) The switching frequency f_{sw}. (b) The dq-axis current i_{dq}.

VI. Conclusion

To maximize the utilization rate of DC voltage, this paper proposes an MPCC method with voltage vector clamping for PMSM to realize overmodulation including six-step operation. The essence of voltage vector clamping is to gradually reduce the space of action of the closed-loop regulation mechanism until it enters six-step mode. It is simple and easy to implement and does not need to add an additional regulator or switch the control framework.

To analyze the current trajectories under different modulation ratios, this paper proposes a coordinate system based on the ideal voltage vector. By analyzing the current trajectory in the ideal voltage reference coordinate system, it is concluded that the horizontal component of the ripple current is obviously larger than the vertical component when the modulation is relatively high. Therefore, an optimal MPCC strategy based on current boundary is proposed. Experimental results showed that six-step operation can be achieved and this strategy has an obvious effect on switching frequency index in the overmodulation area.

References

[1] Z. Zhang, C. Wang, M. Zhou and X. You, "Parameters compensation of permanent magnet synchronous motor in flux-weakening region for rail transit," in *IEEE Transactions on Power Electronics*, vol. 35, no. 11, pp. 12509-12521, Nov. 2020.

[2] Wang, K. Zuo, P. Tao and J. Rodríguez, "High performance model predictive control for PMSM by using stator current mathematical model self-regulation technique," in *IEEE Transactions on Power Electronics*, vol. 35, no. 12, pp. 13652-13662, Dec. 2020.

[3] K. Junejo, W. Xu, C. Mu, M. M. Ismail and Y. Liu, "Adaptive speed control of PMSM drive system based a new sliding-mode reaching law," in *IEEE Transactions on Power Electronics*, vol. 35, no. 11, pp. 12110-12121, Nov. 2020.

[4] H. Yan, Y. Xu, F. Cai, H. Zhang, W. Zhao and C. Gerada, "PWM-VSI fault diagnosis for a PMSM drive based on the fuzzy logic approach," in *IEEE Transactions on Power Electronics*, vol. 34, no. 1, pp. 759-768, Jan. 2019.

[5] Y. Wang, Y. Xu and J. Zou, "Sliding-mode sensorless control of PMSM with inverter nonlinearity compensation," in *IEEE Transactions on Power Electronics*, vol. 34, no. 10, pp. 10206-10220, Oct. 2019.

[6] HOLTZ J, LOTZKAT W, KHAMBADKONE A M, "On continuous control of PWM inverters in the overmodulation range including the six-step mode," *IEEE Transactions on Power Electronics*, 1993, 8(4): 546-553.

[7] KERKMAN R J, LEGGATE D, SEIBEL B J, et al, "Operation of PWM voltage source-inverters in the overmodulation area," *IEEE Transactions on Industrial Electronics*, 1996, 43(1): 132-141.

[8] C. F. Garcia, C. A. Silva, J. R. Rodriguez, P. Zanchetta and S. A. Odhano, "Modulated Model-Predictive Control With Optimized Overmodulation," in *IEEE Journal of Emerging and Selected Topics in Power Electronics*, vol. 7, no. 1, pp. 404-413, March 2019.

[9] A. Sarajian et al., "Overmodulation Methods for Modulated Model Predictive Control and Space Vector Modulation," in *IEEE Transactions on Power Electronics*, vol. 36, no. 4, pp. 4549-4559, April 2021.

[10] A. Brosch, O. Wallscheid and J. Böcker, "Model Predictive Control of Permanent Magnet Synchronous Motors in the Overmodulation Region Including Six-Step Operation," in *IEEE Open Journal of Industry Applications*, vol. 2, pp. 47-63, 2021.

[11] J. ishida, S. Doki and S. Okuma, "Fast Torque Control System of PMSM based on Model Predictive Control Considering Overmodulation Region," *The 2010 International Power Electronics Conference - ECCE ASIA -*, 2010, pp. 1403-1406.

[12] PEI G, LI L, GAO X, et al. "Predictive current trajectory control for PMSM at voltage limit," *IEEE Access*, 2020, 8: 1670-1679.

[13] X. Wang, X. Fang, F. Lin and Z. Yang, "Predictive current control of permanent-magnet synchronous motors for rail transit including quasi six-step operation," *2017 IEEE Transportation Electrification Conference and Expo, Asia-Pacific (ITEC Asia-Pacific)*, 2017, pp. 1-6.

[14] P. Karamanakos and T. Geyer, "Guidelines for the Design of Finite Control Set Model Predictive Controllers," in *IEEE Transactions on Power Electronics*, vol. 35, no. 7, pp. 7434-7450, July 2020.

[15] KHAMBADKONE A, HOLTZ J, "Low switching frequency and high dynamic pulsewidth modulation based on field-orientation for high-power inverter drive," *IEEE Transactions on Power Electronics*, 1992, 7(4): 627-632.

[16] J. Holtz, "Advanced PWM and Predictive Control—An Overview," in *IEEE Transactions on Industrial Electronics*, vol. 63, no. 6, pp. 3837-3844, June 2016.

[17] S. Zhao, X. Huang, Y. Fang and H. Zhang, "DC-Link-Fluctuation-Resistant Predictive Torque Control for Railway Traction Permanent Magnet Synchronous Motor in the Six-Step Operation," in IEEE Transactions on Power Electronics, vol. 35, no. 10, pp. 10982-10993, Oct. 2020.

Xiaochun Fang (S'14–M'17) received the B.S. and Ph.D. degrees in engineering from Beijing Jiaotong University, Beijing, China, in 2010 and 2016, respectively.

He is currently an Associate Professor with the School of Electrical Engineering, Beijing Jiaotong University. His current research interests include traction converters and motor drives, energy management for railway systems, IGBT fault mechanisms, and failure prediction.

Shuai Lin (S'19) received the B.S. degree in electrical engineering from Beijing Jiaotong University, Beijing, China, in 2017, where he is currently pursuing the Ph.D. degree with the School of Electrical Engineering.

His current research interests include motor drives and reliability of traction drive systems.

Xiaofan Wang received the B.S. and Ph.D degree from Beijing Jiaotong University, Beijing China, in 2014 and 2020, respectively, both in electrical engineering.

He is currently a Research Associate with the Locomotive & Car Research Institute, China Academy of Railway Sciences Corporation Limited, Beijing, China. His research interests include traction converter and motor drives, digital control of power-electronic-based devices.

Zhongping Yang (M'14) received the B.Eng. degree from Tokyo University of Mercantile Marine, Tokyo, Japan in 1997, and received the M.Eng. degree and Ph.D. degree from the University of Tokyo, Tokyo, Japan in 1999 and 2002 respectively, all in electrical engineering.

He is currently a Professor in the School of Electrical Engineering, Beijing Jiaotong University, Beijing, China. His research interests include high-speed rail integration technology, traction & regenerative braking technology, and wireless power transfer of urban rail vehicles.

Fei Lin (M'05) received the B.S. degree from Xi'an Jiaotong University, Xi'an, China, the M.S. degree from Shandong University, Jinan, China, and the Ph.D. degree from Tsinghua University, Beijing, China, in 1997, 2000, 2004, respectively, all in electrical engineering.

He is currently a Professor in the School of Electrical Engineering, Beijing Jiaotong University, Beijing, China. His research interests include traction converter and motor drives, energy management for railway systems, digital control of power-electronic-based devices.

Zhongbei Tian (Member, IEEE) received the B.Eng. degree from the Huazhong University of Science and Technology, Wuhan, China, in 2013, and the B.Eng. and Ph.D. degrees in electrical and electronic
engineering from the University of Birmingham, Birmingham, U.K., in 2013 and 2017, respectively.

He is currently a Lecturer in electrical energy systems with the University of Liverpool, Liverpool, U.K. His research interests include railway traction power system modeling and analysis, energy systems optimization, advanced traction power systems design, energy harvesting, and "Rail to Grid" energy systems integration and management.